Magnetically nanostructured state in a Ni-Mn-Sn shape-memory alloy

S. Yuan, P. L. Kuhns, A. P. Reyes, J. S. Brooks, M. J. R. Hoch, V. Srivastava, R. D. James, S. El-Khatib, and C. Leighton

Phys. Rev. B **91**, 214421 — Published 16 June 2015

DOI: 10.1103/PhysRevB.91.214421

Magnetically nanostructured state in a Ni-Mn-Sn shape memory alloy

S.Yuan,[1] P.L. Kuhns,[1] A.P. Reyes,[1] J.S. Brooks,[1,2 †] M.J.R. Hoch[1*], V. Srivastava[3], R.D. James[3], S. El-Khatib[4,5], and C. Leighton[4]

[1]*National High Magnetic Field Laboratory, Florida State University, Tallahassee, Florida 32310, USA*

[2]*Department of Physics, Florida State University, Tallahassee, Florida 32310, USA*

[3]*Department of Aerospace Engineering and Mechanics, University of Minnesota, Minneapolis, Minnesota 55455, USA*

[4]*Department of Chemical Engineering and Materials Science, University of Minnesota, Minneapolis, Minnesota 55455, USA*

[5]*NIST Center for Neutron Research, National Institute for Standards and Technology, Gaithersburg, Maryland 20899, USA and Department of Physics, American University of Sharjah, PO Box 26666, Sharjah, United Arab Emirates*

For certain compositions Ni-Mn-Sn and related magnetic shape memory alloys undergo a martensitic transition at temperatures in the range 300 to 400 K, with the emergence of novel magnetic properties below the transition. While $Ni_{50}Mn_{50}$ is an antiferromagnet, substitution of Sn on some fraction of the Mn sites in $Ni_{50}Mn_{50-x}Sn_x$ leads to competing ferromagnetic (F) and antiferromagnetic (AF) phases at low temperatures. Details of this magnetic phase coexistence are, however, significantly lacking, particularly with respect to the AF phase. The present investigations use zero applied magnetic field ^{55}Mn NMR as a local probe of the magnetic properties of the alloy $Ni_{50}Mn_{50-x}Sn_x$ with x = 10. Rich multi-peak spectra are observed, and the various components are definitively assigned to nanoscale F or AF regions. Measurements of the static nuclear hyperfine field distributions as a function of temperature, and in small applied fields, together with nuclear relaxation rates, provide detailed information on the size distributions, relative concentrations, and physical natures of these F and AF regions. The results show that the nanoscale magnetic features of the x = 10 system are substantially more complex than previous studies have suggested. We argue that the general approach used in these experiments is applicable to other such complex metal alloys, and could yield many additional insights.

PACS numbers : 75.50.Cc, 75.75.Jn, 76.60.Jx

*Corresponding author: hoch@magnet.fsu.edu

† *deceased*

I. INTRODUCTION

The discovery of magnetically induced and largely reversible shape memory effects in Ni-Mn-based alloys has led to considerable interest in these and related materials over the past two decades [1-10]. This activity has been driven both by the fundamental scientific challenges that these systems pose, and by the potential applications of magnetic-field-induced strain effects in sensors and actuators. A number of these Ni-Mn-based alloys undergo a martensitic phase transformation, in certain composition ranges, at temperatures fairly close to room temperature accompanied by a significant reduction in bulk magnetization. The magnetization change enables magnetic field tuning of the transition at temperatures near ambient [2,11-13].

Previous studies of off-stoichiometric $Ni_{50}Mn_{50-x}Sn_x$ alloys have resulted in rich phase diagrams showing the temperature dependences of the various structural and magnetic transitions over a wide range of x [4,5,7]. Small atomic displacements occur at the martensitic transition. The transition temperature, T_m, is strongly x-dependent, falling from 700 K at $x = 5$ to 450 K at $x = 15$. The crystal structure of the $x = 15$ alloy, $Ni_{50}Mn_{40}Sn_{10}$, is monoclinic in the martensitic phase with a large unit cell [5]. As discussed in greater detail below, interesting changes in magnetic properties are found as x is decreased from $x = 25$ (*i.e.* $Ni_{50}Mn_{25}Sn_{25}$), with antiferromagnetic (AF) correlations becoming dominant for $x < 8$ [5,9]. $Ni_{50}Mn_{50}$ is a long-range AF.

Numerous observations point to highly unusual magnetic behavior in these systems, over the composition range $8 \leq x \leq 15$, for which $T_m > 300$ K. The properties include a superparamagnetic-like response in what is a nominally bulk system, as well as a number of phenomena, such as exchange bias (EB), that are suggestive of ferromagnetic (F) and AF competition or coexistence. This microscopic coexistence of F and AF phases below T_m for x in the range 8 – 15 can be understood, in broad terms, by examining the arrangement of magnetic atoms in the lattice (see Fig. 1(a)). (For simplicity small structural distortions linked to changes in x are not shown in Fig. 1.) The lattice constant in the cubic austenite phase of $Ni_{50}Mn_{25}Sn_{25}$ is near 0.605 nm, and the nearest-neighbor (NN) Mn atoms are separated by 0.428 nm. The

F exchange interactions, which are thought to involve an RKKY mechanism, couple the Mn atoms. For the $x < 25$ material, with Mn on some of the Sn sites, mixed phase behavior is found. The NN Mn separation is similar to that of elemental Mn metal and the Mn-Mn coupling is strongly AF (Fig. 1(c)). However, the magnetic couplings between NN Mn atoms are converted from AF to F when, as shown in Fig. 1(b), the central atomic site (labeled site 3) becomes occupied by Sn instead of Mn. Fluctuations in local chemical substitution are then likely to seed local F and AF dominant regions [14], their coexistence leading to the unusual magnetic behavior. While the available evidence suggests that AF correlations are indeed important, particularly in the low temperature martensitic phase [7,9], little is known of the evolution of the AF properties with temperature and composition. As already mentioned, EB effects have been observed in Ni-Mn-Sn, Ni-Mn-Sb and Ni-Mn-In alloys, following cooling to low temperatures (below T_m) [15-18]. The EB observations point to the coexistence of F and AF regions in close proximity to one another. Recent magnetometry experiments on $Ni_{50}Mn_{37}In_{13}$ at low temperatures have provided further important insights [18]. These, and other results, are often qualitatively interpreted within a picture involving superparamagnetic (SP) response due to nanoscale F regions, or clusters, embedded in an AF matrix. The extent to which this AF matrix exhibits long-range order is currently unclear.

Band structure calculations have been carried out for a number of these Heusler-related alloy systems. For example, density functional theory results have been obtained for full-Heusler alloys with composition X_2MnY, where X is typically a transition metal, and Y = Al, Sn, In, Sb *etc*. [19-21]. A *d*- band of itinerant electrons is formed from the Mn and X *d* states. Interestingly, it is shown that *localized* magnetic moments are associated with the Mn sites, as a result of the exclusion of itinerant spin-down electrons from these sites [20]. The Mn moment in a number of the alloys, including Ni_2MnSn, is close to 4 μ_B [19,20]. The energy differences produced by small tetragonal distortions associated with a martensitic-type transition have been obtained for a number of such alloys [21]. Band structure calculations also suggest that a Jahn-Teller (JT) distortion occurs at the martensitic transition in Ni_2MnGa [22]. Support for this JT picture has been provided by polarized neutron scattering experiments which detect changes in the

unpaired electron distribution [23]. The density of states at the Fermi level has been obtained from low temperature specific heat measurements on Heusler alloys, including Ni_2MnSn, and compared with predictions of the local spin density approximation calculations [24]. The experimental value is found to be somewhat higher (~ 60 %) than the theoretical prediction.

Recently, magnetization and neutron scattering experiments have also focused on off-stoichiometric *quaternary* Heusler alloys, such as Ni-Mn-Co-Sn and Ni-Mn-Co-In, in which Co is substituted on the Ni site, resulting in materials with promising properties for technological applications [25-30]. Specifically, they exhibit low thermal hysteresis through the martensitic transition, as well as a large decrease in the magnetization at the transformation, due to a transition from a strongly F austenite to a low temperature state that is weakly magnetic. Related to the above statements, it is not clear whether this low temperature martensite phase is paramagnetic, paramagnetic with AF correlations, or if short- or long-range AF order develops. One significant complicating factor in this regard is the difficulty of determining AF spin structures by neutron diffraction when a potential F to AF transition occurs simultaneously with the martensitic transition to a low symmetry crystal structure [26]. For example, the phase diagram for $Ni_{50-y}Co_yMn_{39}Sn_{11}$, given in Refs. 25 and 31, shows that in the limit $y = 0$ a martensitic phase transition occurs at $T_M \sim 400$ K. This temperature decreases with y, F austenite emerging around $y = 4$-5, the low temperature martensite exhibiting weaker, more complex magnetism, including superparamagnetism, and potentially a superspin-glass phase. A detailed phase diagram for the very similar $Ni_{50-y}Co_yMn_{40}Sn_{10}$ alloys, based on magnetization and neutron scattering measurements [26], confirms that in the range $0 < y < 11$ the martensitic phase indeed exhibits SP properties with a blocking temperature T_B, between 110 and 50 K. In addition, EB effects are found below a blocking temperature T_{EB}. The two blocking transitions are simultaneous at high y, but separate at low y, resulting in a situation at $y = 0$, for example, where SP blocking occurs at $T_B = 110$ K, followed by EB blocking at $T_{EB} = 50$ K [26]. The origin of this "two-stage" blocking is not yet clear. Significantly, however, Bhatti *et al* [14] provided the first direct proof of the existence of nanoscale F clusters at the $Ni_{44}Co_6Mn_{40}Sn_{10}$ composition, deducing *via* small-angle

neutron scattering a liquid-like distribution of nanometric F clusters with a mean center-to-center distance of 12 nm. A compositional fluctuation picture was then advanced to account for F cluster formation [14].

In order to clarify the situation summarized above, in particular to understand the true magnetic structure in the martensitic phases of these alloys, it is necessary to use experimental techniques that can probe the magnetic behavior at a local level, ideally with F/AF specificity. Questions that could then be probed, specifically at the composition studied here, $Ni_{50}Mn_{40}Sn_{10}$, include the nature and morphology of the F and AF regions, their physical sizes, their thermal stabilities, and the details of their interactions with their magnetic surroundings. We emphasize again that even definitive detection of AF order, and some indication of its range, would constitute progress. The present hyperfine NMR experiments in zero applied magnetic field have allowed us to probe a number of these issues. Both F and AF regions are explicitly detected and identified, and their evolution with temperature has been tracked in a representative alloy sample. These results on $Ni_{50}Mn_{40}Sn_{10}$ provide clear information on the nanoscale F and AF components, and permit estimates to be made of their sizes and volume fractions *vs*. temperature. The findings lead, in particular, to an unexpected dual-peaked form for the size distributions of the nanoscale regions, for both F and AF components, suggestive of a morphology not previously considered in these systems. This may provide a means to understand the separation of SP and EB blocking transitions discussed above.

II. EXPERIMENTAL RESULTS AND ANALYSIS

Polycrystalline samples of $Ni_{50}Mn_{40}Sn_{10}$ alloy were prepared by arc-melting high-purity elemental starting materials in Ar. As discussed in more detail in refs. 26, 29, and 31, the samples were annealed in vacuum and subject to characterization by energy dispersive spectroscopy, differential scanning calorimetry, wide angle X-ray diffraction, magnetometry, and small-angle neutron scattering. Further details are provided in these earlier references. For this alloy $T_m \approx 430$ K with a hysteresis width of about

15 K. Importantly, for the NMR experiments presented here the polycrystalline specimens were ground into finer particles and embedded in paraffin wax to allow RF penetration into the metallic grains. As in prior diffraction experiments [26], annealing was performed at 500 - 600 °C in order to relieve any strain introduced by grinding. A frequency-scan pulsed NMR spectrometer was then used to record ^{55}Mn (I = 5/2, $\gamma/2\pi$ = 10.5 MHz/T) spectra in zero field (ZF) using spin-echo techniques at temperature (T) from 1.5 – 380 K.

Figure 2 provides a "waterfall plot" of the ^{55}Mn NMR frequency-sweep spectra for $Ni_{50}Mn_{40}Sn_{10}$, covering the range 150 – 350 MHz, as a function of temperature from 1.6 K to 320 K. NMR signals are found in the range 200 – 350 MHz which corresponds to *static* internal hyperfine fields, $B_{hf} = f_{hf} / (\gamma/2\pi)$, of ~ 19 – 34 T at the ^{55}Mn sites. Assuming that the hyperfine interaction is dominated by the Fermi contact term, we use the form $\boldsymbol{B}_{hf} = -(A/\gamma\hbar)\boldsymbol{S}$ where A is the nuclear hyperfine coupling involving core polarization of the Mn ions by the *d*-electrons with spin $\boldsymbol{S}$ [32]. Transferred hyperfine interactions from neighbor magnetic ions are likely to make some contribution to the net field at a particular site. The observed multipeak spectrum reflects variations in the local electronic structure in F and AF regions of this inhomogeneous metal alloy.[7, 20] Note that the spectra in Fig. 2 have been scaled by T to compensate for the Curie law temperature dependence of the nuclear magnetization. Separate and well identified spectral AF and F peaks, which we will designate AF1 to AF3 and F1 to F3, respectively, are found in the range 240– 340 MHz. In addition, two broad underlying F and AF components, which we will label AF4 and F4, are found for T < 10 K. These spectral designations are explained in detail below, in particular their assignment as "F" or "AF".

As a first step to peak assignment, the NMR signal enhancement factor, $\eta = B_{hf} / B_A$, where B_A is the anisotropy field, was measured at a number of frequencies across these spectra. The enhancement effect in F and AF (*i.e.* magnetically ordered) materials is due to the excitation by the RF field of small angle oscillations of the S spins and thus the associated local hyperfine field. This RF susceptibility effect leads

to an increase in the RF field at nuclear sites and an amplification of the NMR response. Since B_{hf} is obtained from the NMR spectra, and η can be determined by calibrating the RF field using a reference ^{19}F NMR signal, it is possible to determine $B_A = B_{hf}/\eta$. We note as an aside that in this case the values obtained for B_A based on measurements of η are broadly consistent with values obtained from magnetization measurements made on similar alloys [14]. Typically, $B_A = B_{hf}/\eta$ is larger in F than in AF materials. In favorable cases this difference in η allows F spectral components to be distinguished from AF. We find here that η increases by a factor ~ 2 as the frequency is raised from 250 MHz to 330 MHz. While this increase is relatively small, it does suggest that the low frequency spectral components in Fig. 2 are associated with AF regions of the sample, while the higher frequency components are from F regions. Measurements made in small applied fields confirm that this is the case, as explicitly described below. The anisotropy field is correspondingly largest for the lowest frequency components and decreases with increase in frequency from B_A = 0.3 T at 250 MHz to B_A = 0.2 T above 300 MHz, with uncertainties of ~10 %.

To continue the analysis, we point out that the spectra in Fig. 2 can be fit over a wide temperature range using the Gaussian components depicted in Fig. 3(a), and the nomenclature described above. As an example, Fig. 3(b) shows the good fit obtained to the 1.6 K spectrum using these components. Note that below 10 K the two broad components, AF4 and F4, each with full-width at half-maximum (FWHM) ~ 40 MHz, underlie the narrow AF and F components with FWHM ≤ 12 MHz. In the fitting process the various Gaussian component amplitudes were adjusted to allow for the Curie law 1/*T* effect and for any further *T*- dependence due to the evolving spin dynamics and resultant reduction, or even complete disappearance, of a particular component. This fitting process is greatly facilitated by the rapid decrease in amplitude of the broad components AF4 and F4 with increasing *T*. With allowance for the amplitude changes, and for small shifts in frequency of the F components at *T* >100 K (see Fig. 2 and discussion below), excellent least squares fits to the spectra were obtained over the entire temperature range.

The center frequencies obtained from the fit procedure for the narrow F2, F3, and AF2 spectral lines are plotted as a function of temperature in Fig. 4. The small amplitude AF components AF1 and AF3 track the behavior of AF2 exactly, and this suggests that they could be barely resolved ^{55}Mn quadrupolar satellite lines due to electric-field gradients in the non-cubic crystal lattice. Within experimental uncertainty, the AF lines show no detectable frequency shift over the range 1.5 – 300 K, although the Curie-law-corrected (*T*-scaled) amplitudes do decrease markedly with *T*, as described below. The frequencies of lines F2 and F3 on the other hand, are found to decrease slightly with *T* over the range 1.5 – 80 K and then drop more rapidly above about 80 K. This difference in frequency shift behavior of the AF and F lines points to significant differences in the spin dynamics in the sample regions associated with these lines.

The distinction between F and AF regions can be confirmed by the application of an external field, $\mu_0 H_0$, which leads to markedly different trends of the AF and F narrow spectral component center frequencies with increasing H_0. The ^{55}Mn spectral lines from F regions are predicted to shift linearly to lower frequencies, with slope – γ, while, if no spin-flop transition occurs, the AF lines should broaden with increasing field and then split into a doublet. If a spin-flop transition does occur the corresponding AF spectral line will broaden and, in sufficiently high fields, exhibit small shifts to higher frequencies due to slight canting of the spins along the applied field direction. As shown in Fig. 5, which plots the spectral frequencies as a function of applied field at 1.6 K, the components labeled F1, F2, and F3 are clearly F, with the frequencies decreasing linearly as the field is increased above 0.5 T. The straight line fits through the data points in Fig. 5 have slopes – γ, as predicted for a ferromagnet. The gradual increase in frequency of AF2 as the field is increased above 1 T confirms that this line is associated with an AF component in the sample. This behavior suggests that the AF spins undergo a spin-flop transition for $\mu_0 H_0 \leq 1.0$ T, followed by slight canting of the spins for $\mu_0 H_0 > 1.0$ T. We emphasize that these classifications are consistent with those suggested by the η values measured across the spectrum as described above. While

it is not possible to determine the shifts of the broad lines AF4 and F4 in applied fields with the required precision, the η values measured in the wings of these components support the assignations made above. Note that spectra measured in ZF following field-cooling (FC) in 1 T showed no increase in the amplitudes of the F1 – F3 and AF1– AF3 components, but did result in a marked increase in amplitude of the broad underlying disordered components AF4 and F4. The FC increase in signal for AF4 and F4 suggests that, during slow-cooling, field-induced alignment of the spins along *H* (perpendicular to the RF field) occurs in these regions and that the spins remain pinned in ZF. These findings are consistent with the AF4 and F4 regions being comparatively small and being coupled through EB effects at the interfaces. Spin dynamics leads to loss of the NMR signals from these regions at temperatures below T_{EB} from magnetization measurements.

Figure 6 plots the temperature-scaled, and enhancement-factor-corrected composite ^{55}Mn spectral areas, for the AF and F regions, as a function of *T*, in ZF and in an applied field of 1T. Little or no change in behavior is produced by the 1 T field. The observed stepwise decrease in the signal amplitude with *T* is linked to the evolving *S* spin dynamics in the various regions. The plotted areas were obtained by integrating the spectra in two major intervals, firstly above 270 MHz (F) and, secondly below 270 MHz (AF). The spectra in these two frequency ranges were recorded at different RF power settings (which were obtained by adjusting the pulse amplitude to maximize the spin echoes in the two ranges) in order to allow for the difference in η values. The normalized spectral areas in Fig. 6 permit estimates to be made of the fractions of the Mn sites that are in F and AF ordered regions as a function of temperature. These estimates are presented and discussed in Section III below. We point out that it is likely that a small fraction of the Mn atoms are located in regions that remain dynamic on the NMR timescale even at the lowest temperatures probed in the present experiments. The dashed vertical line at 7 K in Fig. 6 separates the low temperature region, labeled region I, in which the amplitudes of the broad components AF4 and F4 steadily decrease, from the high temperature region, region II, in which the amplitudes of the remaining components show plateau features. This behavior is discussed in detail below.

Measurements of the ^{55}Mn spin-lattice, T_1, and spin-spin, T_2, relaxation times have also been made, over a wide temperature range. The T_1 values for the F3 and AF2 spectral components are plotted versus T in Figs. 7(a) and 7(b) respectively. The vertical dashed lines at 7 K again separate regions I and II which exhibit distinctly different types of T_1 behavior. As can be seen for F3 in Fig. 7(a) the application of a magnetic field of 1T produces a small increase in T_1, by a factor ~ 2, in region I and even smaller changes in region II. In contrast, the T_1 values for AF2 in Fig. 7(b) show little field-induced increase in region I, but a significant increase in region II. Note that at low temperatures (T < 10 K) the underlying broad spectral components AF4 and F4 contribute a major part of the observed NMR signals at the center frequencies of AF2 and F3. The measured T_1 values thus represent averages of contributions from distinct regions, with different sizes, as discussed in full in Section III below. The observed nuclear magnetization recovery curves for both F and AF components exhibit stretched exponential behavior described by $\left(1-e^{(-t/T_1)^{\beta}}\right)$ with $\beta \leq 1$. This form reflects the inhomogeneous nature of the sample, with the various sized regions giving different relaxation behaviors at a given temperature. At the lowest temperatures T < 4 K, where the small regions are of dominant importance, we find $\beta < 1$ with lower values for the F than for the AF component. Low β values indicate a broader distribution of relaxation times than do high β values. In the F case as T is raised, in region I, from 1.5 – 7 K, β decreases to ~0.5. This decrease occurs as the signals from the F4 regions become of diminishing importance but still observable. An increase in β occurs in region II, above 10 K, as the larger F regions become of dominant importance in determining the NMR signal amplitude. The variation of β with increasing T is less pronounced for the AF component (inset to Fig. 7(b))) than for the F component. This difference in behavior reflects the greater proportion of large regions in the AF case than in the F case.

Figures 8(a) and 8(b) show the transverse spin-spin relaxation time, T_2, for components F3 (plus F4) and AF2 (plus AF4) as a function of T. The T_2 values for F3 are considerably shorter than those of AF2 and show greater variation with temperature below 20 K. The spin-echo decay curves in this case show

marked stretched exponential behavior with β values given in the insets to Fig. 8(a) and Fig. 8(b). Following a sharp decrease in region I to below 0.5, the β values for F3 steadily increase with rising temperature in region II. This behavior shows that the distribution of T_2 values initially broadens and then narrows again as the underlying F4 component diminishes in importance. In contrast, the β values for AF2 exhibit a shallow minimum near 4 K followed by a marked decrease above 20 K. Note that at a given temperature the T_2 values for both F3 and AF2 in Fig. 8 are roughly two orders of magnitude shorter than the corresponding T_1 values in Fig. 7.

The stretched exponential relaxation behavior that is observed, particularly at low temperatures, suggests that the dynamic spin regions, which are responsible for the fluctuating local fields involved in relaxation processes, have a distribution of correlation times. In the present experiments the spin-echo measurement timescale is $\tau_m^{NMR} \sim 20$ μs. It follows that hyperfine field fluctuations with short correlation times in particular regions of the sample lead to the loss of the corresponding *I* spin contributions to the ^{55}Mn spin-echo signal when $T_2 < \tau_m^{NMR}$. Spin-echo signals are obtained exclusively from the long correlation time *effectively static* regions where $T_2 > \tau_m^{NMR}$. The relaxation time results are discussed in Section IIID.

III. DISCUSSION

The ZF ^{55}Mn spectra in Fig.2, which exhibit distinct narrow features in the F regions, for $f > 270$ MHz, and in the AF regions, for $f < 270$ MHz, are a powerful source of information on the nanoscale magnetic properties of $Ni_{50}Mn_{40}Sn_{10}$. The designation of the various spectral features as AF or F in origin is primarily based on frequency shifts of the narrow components with applied field, and with temperature, as described in Section II. The estimated anisotropy fields obtained from measurement of the η values at selected frequencies provide support for the assignments.

We note at this point that recent ^{55}Mn NMR experiments on three differently prepared samples of the F full Heusler alloy Ni_2MnGa have provided information, derived from η, on the anisotropy field for temperatures above and below the martensitic transition in that compound at $T_M \sim 200$ K [33]. For all three samples the spectra at 5 K show a dominant peak at 315 MHz which shifts to lower frequencies as the temperature is raised. Small structural features in the spectra are attributed to *austenite* remnants which persist down to 5 K. The resonance frequency for the dominant spectral component is close to that found for F2 and F4 in the present experiments. The spectra are, in fact, similar to those obtained in earlier ^{55}Mn NMR experiments on Ni_2MnSb [34]. Neither of these investigations on the ferromagnetic full Heusler alloys showed spectral components in the range 200 – 300 MHz, however, where strong lines attributed to AF regions are found in the present experiments on $Ni_{50}Mn_{40}Sn_{10}$. The components definitively assigned to AF regions in the current work thus emerge when the Mn content is driven away from 25 atomic %. This conclusion is consistent with the concepts summarized in the Introduction, *i.e.* that AF Mn-Mn interactions are introduced when excess Mn occupies Sn sites. Figs. 2-5 thus provide solid evidence of truly AF regions in $Ni_{50}Mn_{40}Sn_{10}$ at low T, a significant finding. Further analysis below will elucidate the length scales associated with these regions (as well as the F regions).

A. Ferromagnetic and antiferromagnetic spectral components

The behavior with temperature of the scaled areas of the low frequency (<270 MHz) ^{55}Mn spectral components given in Fig. 6 indicates that there are two distinct types of AF components with very different spin dynamics. These two AF components exhibit NMR spectral area transitions with midpoint temperatures in the transition regions of $T \sim 4.5$ K (region I) and $T \sim 260$ K (region II), *i.e.* temperatures well below the martensitic phase transition temperature $T_M \sim 400$ K. Similarly, for the high frequency (>270 MHz) F components, Fig. 6 suggests there are again two types of regions, with spectral area transitions occurring at midpoints of $T \sim 3$ K and $T \sim 150$ K. As will be returned to, the midpoints of the lower T transitions in the F and AF components (3 and 4.5 K) are thus almost coincident, whereas the higher T transitions are not (150 and 260 K).

The observed distribution of frequencies in the ^{55}Mn spectra, which exhibit multiple peaks, with both broad and narrow components, clearly points to a distribution of hyperfine fields at nuclear sites in different regions of the sample. The hyperfine field distribution is attributed to variations in the local electronic structure, likely linked to statistical fluctuations in the local Mn concentration, particularly at the interfaces between F and AF regions. These effects produce variations in the hyperfine field and result in line broadening. Similarly, the shift of the AF components to lower frequencies than those of the F components is again attributed to differences in the local electronic structure of the corresponding Mn sites. The NMR spectra suggest that local aggregates of the Mn atoms that substitute Sn sites determine the structure and geometrical forms of the magnetically distinct F and AF regions.

Importantly, the spectral area data of Fig.6 allow estimates to be made of the volume fractions of the NMR-detected F and AF magnetic regions as a function of temperature. At 1.6 K we obtain 45 % F and 55 % AF, with uncertainties of ±5 %. In the range 4 to 10 K the AF fraction decreases by a factor ~2, corresponding to the loss of the broad AF4 contribution, while the F component decreases by a factor ~4 due to the complete loss of F4 and 50 % loss of F1, F2, and F3. The fraction of the sample that is F above 10 K is therefore only ~12 %. In essence, the transition from region I to region II is accompanied by a much larger loss in F volume fraction than AF volume fraction. Most importantly, these data reveal, very clearly, two distinct types of both F and AF regions, with very different local environments and thermal stabilities. Explicitly, a large fraction of the F regions become thermally unstable around 3 K, the remainder only doing so at 150 K. Approximately half of the AF regions also transition in the range 3-5 K, whereas the remainder are stable to a much higher temperature, around 260 K. Similarly, Figs. 7 and 8, which show clear changes in behavior at the region I / region II boundary, reveal that these two types of F and AF regions also have very different spin dynamics. One simple interpretation of this behavior is a doubly-peaked (*i.e.* bimodal) distribution of sizes of both F and AF clusters in this system. This is clearly of interest both in terms of the above-summarized evidence for F clusters in these alloys, leading to SP behavior, and the "two-stage" blocking phenomenon in $Ni_{50}Mn_{40}Sn_{10}$, where T_{EB} and T_B become separated

[26]. Before discussing further the nature of the various magnetic regions detected here, which may include the F clusters responsible for SP behavior, we firstly review the expected dynamical behavior of SP clusters in order to illuminate the discussion.

B. Modeling superparamagnetic cluster dynamics

Conventional theoretical treatments of SP clusters involve the magnetocrystalline anisotropy energy of a cluster of volume V, which is expressed in terms of the angle θ between the cluster magnetization vector and the crystal easy axis, and has the form $E_A = K_A V \sin^2\theta$ with K_A the anisotropy energy density [35, 36]. We are assuming here uniaxial magnetocrystalline anisotropy. For small θ we obtain $\theta_m^2 = K_A V / k_B T$ with θ_m^2 the mean square amplitude of the collective spin oscillations. As T is raised thermally activated flips of the cluster magnetization (macrospin) between the two energy minima occur, with a T-dependent correlation time, τ, governed by the Néel-Arrhenius relation

$$\tau = \tau_0 \exp\left(\frac{K_A V}{k_B T}\right). \qquad (1)$$

The pre-exponential characteristic time τ_0 (*i.e.* inverse attempt frequency), is in the range 10^{-9} to 10^{-10} s [14]. The conventional SP blocking temperature at which the experimental measurement characteristic time $\tau_m = \tau$ is then given by

$$T_B = \frac{K_A V}{k_B \ln\left(\tau_m / \tau_0\right)}. \qquad (2a)$$

For $T > T_B$ the cluster *composite* spin undergoes $\theta = 180^{\circ}$ reorientations with $\tau < \tau_m$. At temperatures well below T_B the cluster magnetization executes only small angle collective oscillations about the easy axis at frequency $1/\tau_0$. The frequency is weakly temperature dependent as the mean amplitude $\theta_m(T)$

increases with *T*. Importantly, in ZF NMR experiments of the type presented here, the nuclear signals are no longer detectable when $T_2 \le \tau_m^{NMR}$, as pointed out in Section II. The effective NMR blocking temperature, denoted T_B^{NMR}, which corresponds to the temperature at which the loss of signal occurs, follows from the expression for $1/T_2$ given in Eqs. (A1) and (A2) in Appendix A where $\omega_S = 2\pi/\tau_0$, $\omega_I = 2\pi f_{hf}$ and τ_C the spin cluster correlation time for thermal interaction with the lattice. We obtain

$$T_B^{NMR} = \frac{\sqrt{12}}{\sqrt{S(S+1)}}\left(\frac{1}{\omega_I}\right)\left(\frac{K_A V}{k_B}\right)\left(\frac{1+\omega_S^2\tau_C^2}{\tau_C\tau_m^{NMR}}\right)^{1/2} \approx \sqrt{2}\left(\frac{\omega_S}{\omega_I}\right)\left(\frac{K_A V}{k_B}\right)\left(\frac{\tau_C}{\tau_m^{NMR}}\right)^{1/2}. \qquad (2b)$$

The approximation in Eq. (2b) holds for $\omega_S\tau_C > 1$ and taking $S = 2$ for the Mn ion. (The expression for $1/T_2$ from Appendix A, is given in Eq. (4) below.) It is interesting, and important, to note that T_B^{NMR} can be similar to T_B from DC magnetometry measurements in spite of the very different timescales involved in the DC and RF measurements. The similar values for the two blocking temperatures suggested by the present experiments can be explained by considering the ratio $T_B^{NMR}/T_B = \sqrt{2}\ln(\tau_m/\tau_0)(\omega_S/\omega_I)(\tau_C/\tau_m^{NMR})^{1/2}$ and by assuming that at T_B^{NMR} the cluster $\tau_C \approx \tau_m^{NMR}$ and inserting numerical estimates for the other quantities. This apparently counter-intuitive similarity in blocking temperatures occurs because at T_B^{NMR} the intra-well collective oscillations of a SP cluster reach a critical amplitude $\theta_m^{crit}(T_B^{NMR}) \approx 180^{\circ}$, which leads to nuclear magnetization dephasing on the 10 μs timescale with loss of the spin-echo signal. At T_B^{NMR} infrequent 180° flips may take place on a long time scale, of the order of 100 s, as detected in magnetization measurements.

Another important feature in characterizing nanoscale magnetic clusters *via* NMR involves changes in the hyperfine field with temperature due to averaging effects linked to collective spin excitations. Mössbauer

spectroscopy has been used to study this effect in a number of systems [35, 36]. Using Boltzmann statistics it can be shown that the dominant $q = 0$ uniform SP cluster mode leads to a linear decrease in the hyperfine field with T given by

$$B_{hf} = B_0\left[1 - \frac{k_B T}{2K_A V}\right], \tag{3}$$

provided that $k_B T \ll K_A V$ [35]. For the present ZF NMR experiments the measured frequency $2\pi f_{hf} = \gamma B_{hf}$ should therefore, at sufficiently low temperatures, decrease linearly with temperature with slope given by $-\left(k_B / 2K_A V\right)$. In ZF NMR experiments the dynamic hyperfine field is not detectable (*i.e.* is effectively zero) for $T > T_B^{NMR}$. When an external magnetic field is applied to a SP system the cluster energy expression is modified by the inclusion of an additional term and takes the form $E_A = K_A V \sin^2\theta - \mu_0 m H_0 \cos\left(\alpha - \theta\right)$, with the N–spin cluster magnetic moment given by $m = N\mu$. In low applied fields with $\mu_0 m H_0 < K_A V$ ($\mu_0 H_0 < 1$ T in the present experiments) the angle α between the applied field and the easy axis of a cluster should be averaged over a sphere for a polycrystalline sample. In higher fields, with $\mu_0 m H_0 > K_A V$, the dynamics of SP-F clusters will be modified and, at a given T, the probability of large angle flips will decrease, leading to a shift in the conventional T_B to higher temperatures. For SP-AF clusters the situation is somewhat different since the application of a field may lead to a spin-flop transition, and some subsequent canting of the cluster spins along the applied field direction.

In applying these cluster model ideas to the present results we note that a major advantage of the ZF NMR approach arises from the direct determination of B_A using the measured enhancement factor η, together with the relation $\eta = B_{hf} / B_A$ introduced above. From B_A the anisotropy energy density $K_A = \frac{1}{2} n\mu B_A$ is obtained using the spin density n and the localized moment $\mu \approx 4\mu_B$. This procedure is

applicable to both F and AF systems. For $Ni_{50}Mn_{40}Sn_{10}$, the anisotropy fields obtained from the measured η values are 0.3 T for AF and 0.2 T for F. The corresponding energy densities are K_{AF}~ 1.0 x 10^6 erg/cm^3 and K_F~ 6.8 x 10^5 erg/cm^3.

The contributions to the ^{55}Mn longitudinal and transverse relaxation times due to the fluctuating hyperfine field in a cluster of volume V, at temperatures $T << T_B$, are discussed in Appendix A. It is shown there that the intra-cluster spin dynamics make no contribution to T_1 but play an important role in determining T_2. The following expression, given in Eq. (A2), is obtained for the spin-spin relaxation rate in the long correlation time limit for $S = 2$

$$\frac{1}{T_2} = \tfrac{1}{2}\left(\frac{\omega_I^2}{\omega_S^2}\right)\left(\frac{T}{T^*}\right)^2\left(\frac{1}{\tau_c}\right), \tag{4}$$

with $\omega_I^2 = \left(A/\hbar\right)^2$, $\omega_S^2 = \left(2\pi/\tau_0\right)^2$, $T^* = K_A V/k_B$. The correlation time, τ_c, which is determined by coupling of the cluster spin to the lattice, involves phonon-scattering-induced changes in the cluster-spin oscillation amplitude and phase. For a SP globular cluster of volume V, taking τ_0 =10^{-9} s and, for the present NMR experiments, τ_m = 2x10^{-5} s, the characteristic temperature T^*, introduced above, is obtained in terms of T_B as $T^* \approx 25T_B$. The Néel-Arrhenius expression can be written as $\tau = \tau_0 \exp\left(T^*/T\right)$. Marked changes in $1/T_2$ are therefore expected as T/T^* increases, and τ_c decreases.

For a material with a range of SP cluster volumes, described by a probability distribution $P(V)$, there is corresponding distribution of T_B^{NMR} values. The amplitude of the NMR signal from a system of this type will decrease as the temperature is raised and fewer and fewer clusters contribute to the signal. Statistically the decrease is described by the Poisson distribution and it follows that the signal decays as $S(T) = S_0 \exp\left(-\tau_m/T_2\right)$ where $S(T)$ is the signal amplitude at temperature T and S_0 the low

temperature amplitude. The value of T_2 is obtained using Eq. (4). By numerical integration over the volume distribution it is possible to fit the experimental results as shown in Section III C. In applying this procedure to data it is necessary to choose an expression for the *T* dependence of the correlation time τ_c. We have found that a modified Néel-Arrhenius expression, with a somewhat reduced T^* value, works very well. The cluster size distributions that are obtained are robust to changes in the parameters that are used in the fit process.

C. Superparamagnetism in $Ni_{50}Mn_{40}Sn_{10}$

The concepts reviewed and developed in sub-section B can now be applied to analyze the data. We first consider the two broad underlying F4 and AF4 components (Fig. 3) that are observed at temperatures below 10 K (Fig. 6). The broad frequency distributions and the marked *decrease* in the spectral areas with increase in temperature for these components, as shown in region I of Fig. 6, complicate the discussion of the size and nature of these regions of the sample, which contribute ~50 % of the observed ^{55}Mn NMR signal for $T < 2$ K. Because of the large linewidths of AF4 and F4, and the limited temperature range (1.6 – 10 K) over which their spectral amplitudes decrease to zero, it is not straightforward to determine whether or not these components are exhibiting SP blocking behavior. Indeed, these regions may not be small volume globular SP clusters but instead extended F and AF boundary layers in close proximity to each other. Interface regions of this type are in fact needed to explain the EB effects that are detected below 50 K [18]. Strong evidence for this suggested proximity of F and AF regions is provided by the very similar forms obtained for the decrease in integrated signal areas with temperature below 10 K as shown in Fig. 6 for the two components. The observed increase in amplitude of components AF4 and F4, by a factor ~ 3, in FC experiments further points to field-induced *alignment* of spins along *H* (perpendicular to the RF field, H_1) during cooldown together with pinning of the AF spins in ZF as required for EB. The cooling field dependence of the EB shift in Heusler-type alloys is non-trivial and has not been pursued in detail in the present experiments.

Turning to the F components which persist to $T > 150$ K (Fig. 6), we note that over a limited temperature range (4 K < T < 50 K) values of the F2 and F3 spectral frequencies, as shown in Fig. 4, decrease steadily and almost linearly with T (see inset in particular). This finding is consistent with the behavior predicted for SP clusters at sufficiently low temperatures as given by Eq. (3). The solid straight line in Fig. 4, which follows the trend of the plotted points, in fact has slope given by $k_B/2K_AV = 1/2T^*$ with V taken as the volume of a spherical cluster of diameter $d \approx 10.6$ nm. This size estimate is based on previous magnetometry results, which give $T_B \approx 110$ K for this composition [26], and use of Eq. (2a) with the DC measurement time $\tau_m \sim 100$ s. The consistency between the NMR temperature-driven frequency shift and DC magnetization measurements is thus very good, implying that the thermal evolution of the F spectral components is consistent with the SP blocking of the nanoscale F regions claimed from earlier work [26]. Further evidence for this conclusion is provided below.

By allowing for a distribution of cluster sizes, in a simplified spheroidal SP cluster model, it is possible to also obtain a good description of the data of Fig. 6, *i.e.* not only the T dependence of the frequency, but also the T dependence of the F component's scaled intensity. This was done, following the procedure described in Section III B, by numerical integration over a bimodal Gaussian distribution of cluster sizes with a corresponding distribution of T_B^{NMR} values. The fits obtained are shown in Fig. 6. The F region II component, to which this model is best suited, is fit (solid line) with a Gaussian distribution centered at a cluster diameter $d_{II} \approx 8.4$ nm, with FWHM $\delta_{II} \approx 4.0$ nm. Note the very reasonable consistency between this value, in the range 4 – 12 nm, compared to the 10.6 nm extracted from magnetometry and from the T dependence of the NMR frequency of the F spectral components as given above. In region I the corresponding fit values, which correspond to a *half-Gaussian* distribution, are $d_I \sim 0$ nm and $(\delta_I/2) \sim 1.2$ nm. We emphasize that these region I parameters are physically less meaningful than those in region II, because the cluster geometry in region I is probably not spheroidal. As discussed explicitly above, the region I blocking transition is likely associated with surfaces of F/AF interaction, meaning that the

dimensionality of the region I blocking is also different to the region II blocking. A similar fit procedure involving a bimodal distribution of cluster sizes was applied to the AF data in Fig. 6. The simple spheroidal SP model is, at best, a crude approximation for these AF regions since, as mentioned above, the AF components I and II are unlikely to approximate spheroids. The region I blocking is likely 2D in character, while the region II blocking is likely associated with AF regions surrounding F clusters, consistent with the discussion in the Introduction. The latter point will be returned to when the *T* dependence of the AF frequencies is discussed. The fit curve (dashed line) through the data points should thus be regarded as a guide to the eye, or, at best, a qualitative description.

Returning to frequency shifts, inspection of Fig. 4 shows that for $T > 50$ K the frequencies of the F components decrease more rapidly with *T* than the prediction of Eq. (3). The dashed line curves through the points are in fact spline fits and are simply guides to the eye. The observed curvature may be due to the gradual breakdown of the low temperature approximation for SP cluster dynamics. An alternative explanation for the observed frequency drop is thermal disordering of the spins within a fraction of the clusters. We note in this regard that an attempted Brillouin function fit (not shown) to the F3 frequency data in Fig. 4 is not in agreement with the plotted points. The available evidence does not permit a distinction to be made between the two possible explanations for the nonlinear decrease in f_{hf} above 50 K, and it is certainly possible that both of these effects play a role.

Turning to the AF2 component behavior displayed in Fig. 4 we see that f_{hf} has no detectable *T*-dependence up to 350 K. This *T*-independence of the frequency is also found for the two satellite components, AF1 and AF3. Note that it is the frequency of the *remnant* AF2 regions that is displayed in Fig. 4 and that over the range 150 to 350 K the Curie-law-scaled AF ^{55}Mn signals steadily decrease, as can be seen in Figs. 2 and 6. This *T*-independence of the frequency is clearly inconsistent with the linear decrease in *f* with *T* expected for globular clusters. This feature suggests that the AF regions consist of extended structures, which gradually reduce in volume as a fraction of the *S* spins, located in subregions

which may be weak links in chains or other extended structures, become increasingly dynamic on the NMR timescale. In this picture the extended structures constitute what has been termed the "AF matrix" in interpretations advanced in earlier works.

D. Nuclear relaxation

The discussion here will focus on the interpretation of the spin-lattice relaxation rate behavior with temperature (Fig. 7). As shown in Section II B, the spin-spin relaxation times reflect the hyperfine field fluctuations associated with collective spin dynamics in F or AF regions. It follows that T_2 is closely related to the changes in spectral amplitude shown in Fig. 6, and is of key importance in determining T_B^{NMR}. In contrast, T_1 is determined through other degrees of freedom in the system.

The temperature dependence of the ^{55}Mn $1/T_1$ values, measured in fields of 0 T and 1 T at frequencies which correspond to the major components F3 and AF2, are shown in Figs. 7(a) and (b), respectively. It must be borne in mind that at low temperatures, below 10 K, the underlying broad spectral components F4 and AF4 contribute a major part of the observed NMR signals at the center frequencies of F3 and AF2. Below 10 K the measured relaxation times are therefore averages over the size distributions. As mentioned in Section II, both F and AF nuclear magnetization recovery curves exhibit stretched exponential behavior with the exponent values β shown as insets in Figs. 7(a) and (b). The stretched exponential form reflects the inhomogeneous nature of the sample, with regions of different sizes and geometries giving different relaxation behaviors at a given temperature. At the lowest temperatures $T < 7$ K, denoted region I, as in Fig. 6, where smaller regions are of dominant importance, we find $\beta \approx 0.75$ for the AF signals and $\beta \approx 0.55$ for the F. As T is raised, β increases gradually in both cases, consistent with a narrower distribution of relaxation times in region II. The variation of β with temperature for the T_1 processes in Fig. 7 is less marked than for the T_2 relaxation in Fig. 8. Note also that the AF T_1 values are more than an order of magnitude larger than those of the F components. The fitted curves in Figs. 7(a) and 7(b) are discussed below.

The forms of the relaxation rate transition regions in Figs. 7(a) and (b) are similar to those shown for the F and AF component spectral areas displayed in Fig.6. This similarity in behavior with temperature suggests that the physical mechanisms that operate in both F and AF regions are related, and involve regions with a distribution of sizes. The smaller regions produce fluctuating dipolar fields in larger neighbors thereby providing a spin-lattice relaxation mechanism. It appears likely that at low temperatures disordered surface regions at the interface between F and AF components constitute dynamic shell or boundary structures adjacent to larger interior regions from which the NMR signals are detected. As T_2 for regions of volumes V decreases with increasing T, as predicted by Eq. (4), fewer and fewer clusters meet the $T_2 > \tau_m^{NMR}$ criterion and a transition occurs on the NMR timescale resulting in the loss of spin-echo signals from these clusters. Again we emphasize that it is convenient to use the term "cluster" to denote distinct groupings of spins in distinct F and AF regions, but the cluster geometry is not entirely clear and is not necessarily globular in form.

Since intra-cluster fluctuations in the hyperfine field do not contribute to spin-lattice relaxation, as discussed in Appendix A, two other ^{55}Mn spin-lattice relaxation mechanisms are considered: (*i*) Korringa-like (or Korringa – Moriya) relaxation *via* the itinerant conduction electrons, and (*ii*) inter-cluster dipolar interactions involving relatively small dynamical clusters in proximity to larger structures whose spins are effectively static on the timescale of the NMR experiments. These mechanisms are discussed in Appendix B.

It appears that both mechanisms (*i*) and (*ii*) contribute to relaxation. The Korringa-Moriya process for F metals, which predicts $1/T_1 \propto T$, is of dominant importance at $T > 10$ K, where the large clusters contribute the major portion of the measured NMR signal, while the inter-cluster fluctuating dipolar field mechanism is of primary importance at lower T, where contributions from smaller clusters to the spectra prevail. The fluctuating dipolar field produced by rapidly flipping small clusters containing N spins, and with magnetic moment $N\mu$, falls off as $1/r^3$. A straightforward calculation shows that the inter-cluster

dipolar mechanism becomes ineffective for nuclei in large clusters with dimensions estimated as $d > 3$ nm. The two independent processes are combined to give the average spin-lattice relaxation rate in a *particular spin cluster category*, made up of clusters of the same volume, as

$$\frac{1}{T_1} = \left(\frac{1}{T_1^{inter}}\right) + \left(\frac{1}{T_1^{K}}\right). \tag{5}$$

For small clusters with $d < 3$ nm the first term in Eq. (5) is expected to be dominant, while for the larger clusters the second term will play the major role.

As discussed in Appendix B it is convenient to introduce the quantities $F_{sc}(T)$ and $F_{lc}(T)$ to represent the temperature-dependent fractions of the sample in small cluster, *sc*, or large cluster, *lc*, categories which together give rise to the NMR spin-echo signals. For $T < 10$ K, $F_{sc} > F_{lc}$ and the intercluster dipolar mediated mechanism is most important, while for $T > 10$ K we have $F_{sc} < F_{lc}$ and the Korringa mechanism becomes dominant, as shown below. Expressions for T_1^{inter} and T_1^{K} are given in Appendix B.

The fitted curves in Figs. 7 (a) and (b) were obtained using a combination of the Redfield and Korringa relationships, as presented in Appendix B, to describe relaxation processes in semi-quantitative terms in this highly inhomogeneous system. Firstly, it is convenient to plot the data in the form $1/(T_1 T)$ versus T as shown in Fig. 9(a) for the F case, and Fig. 9(b) for the AF case. The fit parameters used in Figs. 9(a) and (b) are then used in Figs. 7(a) and (b), respectively. In the fit process we determined $1/(T_1 T)$ as a weighted sum of the contributions shown in Eq. (5), together with the expressions given in Eqns. (B1) and (B2). We assume that $1/T_1^{K}$ is the same for all clusters. As an approximation, a distribution consisting of three dynamic cluster volumes is used, together with a modified version of Eq. (1) (allowing for the change from T_B to T_B^{NMR}), to model $P(\tau)$ in Eq. (B1). In the fit process we take $\tau_0 = 10^{-10}$ s and the amplitude of the ensemble average component of the fluctuating dipolar field perpendicular to B_{hf} is found to be $B_{\perp}$ =

0.09 T. This value is consistent with an order of magnitude estimate based on $B_{\perp} \sim N_C \mu / \langle r \rangle^3$ where N_C ~ 100 is taken as the average number of spins in a small dynamical cluster located at a distance $\langle r \rangle$ ~ 2 nm from an effectively static cluster that contributes to the observed ^{55}Mn signal.

A similar approach to that used for F3 together with F4 has been used to analyze the T_1 data for the components AF2 plus AF4, as shown in Fig. 9(b) which plots $1/T_1T$ versus T for the AF components. As already mentioned, the AF2 component spin structures are likely to consist of extended regions, rather than globular clusters, and Fig. 9(b) shows that T_1 in these regions is dominated by the Korringa mechanism for $T > 20$ K, analogous to the F component case in Fig. 9(a).

In region I the inter-cluster dipolar mechanism is of primary importance due to the evolving cluster dynamics for spins in the AF4 regions. If these simple cluster model ideas are applied in this T range then the fit process based on Eqn. (B1) leads to $B_{\perp}$ ~ 0.03 T, which is a factor 3 smaller than for the F component. This decrease in the fluctuating local field in the small cluster regions points to smaller net moments in the fluctuating shell regions adjacent to the core clusters which contribute to the NMR signal. Note that in region II, where the Korringa mechanism plays a dominant role for AF2, as shown in Fig. 9(b), the value of $1/T_1T$ is roughly an order of magnitude smaller than for F3. This suggests that the density of states at the Fermi level is smaller by a factor ~3 in the AF regions compared to the F regions.

The application of a magnetic field to a polycrystalline ferromagnetic material, in which the easy axes in each crystallite are distributed over a sphere, can induce a change in P and hence $B_{\perp}$. This field effect permits the relative importance of the Redfield (field-dependent) and Korringa (field-independent) mechanisms to be estimated. While the observed field-dependences are not marked for an applied field of 1 T, the plots in Figs. 7(a) and (b) are consistent with the Redfield mechanism playing a role at low T, where small clusters contribute significantly to the observed NMR signal, and fluctuating dipolar fields are produced by still smaller dynamic clusters. As T is raised the fluctuating dipolar mechanism decreases

in importance for the F component, as F_{sc} tends to zero. In contrast, T_1 for the AF component is field-dependent in region II. The marked difference in the field dependences of the F and AF components is attributed to the difference in the itinerant electron Korringa contribution, which, as seen in Figs. 9(a) and (b), is enhanced by more than an order of magnitude in the F clusters compared to the AF.

An estimate of the density of states at the Fermi level for the F3 component can be obtained from the Fig. 9(a) experimental value $1/T_1T = 50$ s^{-1}K^{-1}. In Eq. B2 we take $\left\langle 1/r_A^3 \right\rangle_F = 4.79$ a.u. (0.32 x10 ^{32} m^{-3}), and assume that $\rho_{\downarrow}^2 \approx 0$ at ^{55}Mn sites because spin down electrons are excluded from these sites [20], which allows us to replace $\rho_{\uparrow}^2 + \rho_{\downarrow}^2$ by $\rho_{\uparrow}^2$. We thus obtain $\rho_{\uparrow} = 1.4$ (eV f.u.) $^{-1}$ which is quite consistent with density functional theory estimates in the range 0.9 - 1.5 (eV f.u.) $^{-1}$ for majority spins in Ni_2MnSn [19,20]. Specific heat measurements for Ni_2MnSn give the total density of states as $\rho(E_F) = 4.4$ (eV f.u.) $^{-1}$ [24]. The similarity of the present estimate of $\rho_{\uparrow}$ for $Ni_{50}Mn_{40}Sn_{10}$ with the values given in the literature for related alloys supports the conclusion that the Korringa mechanism is of dominant importance in spin-lattice relaxation for $T > 20$ K.

The relaxation time analysis given above is based on a simple cluster model, and is at best semi-quantitative. However, the fit results shown in Figs. 7(a) and (b) clearly support the approach we have used. The findings are consistent with the dual-peaked- size distributions of both F and AF regions in $Ni_{50}Mn_{40}Sn_{10}$ that are introduced in considering the scaled spectral areas plots in Fig. 6, as presented in Section III A. Note that it is likely that a small fraction of the spins located in very small clusters remain dynamic and undetected in the present experiments, even at 1.5 K. While the precise physical origin of the deduced size distribution remains to be explored, the present model provides a basis for explaining other magnetic properties, such as EB, of the $Ni_{50}Mn_{40}Sn_{10}$ alloy, in which competing F and AF interactions are of key importance.

IV. CONCLUSIONS

The present experiments show that ZF hyperfine NMR is a powerful technique for investigating the complex nanoscale magnetic behavior of off-stoichiometric Heusler alloys. The ^{55}Mn spectra obtained as a function of temperature for the representative alloy $Ni_{50}Mn_{40}Sn_{10}$, reveal rich detail with distinct spectral features for F and AF regions in the sample. The resonance frequencies of the spectral components are determined by the different hyperfine fields experienced by nuclei in the various local electronic environments in this material.

The results obtained for $Ni_{50}Mn_{40}Sn_{10}$ reveal *two* separate magnetic transitions in the martensitic phase for both the F and AF components. For the local F regions the transitions resemble blocking transitions as detected in magnetization measurements on SP systems. The lower T transition is attributed to F interface spins at F/AF boundaries, with 2D surface/interface characteristics. The transition at higher T is associated with large F regions or clusters. NMR signals from the AF components are also consistent with two different sized regions, again likely of different dimensionality.

Based on the NMR spectra, estimates are made of the volume fractions of the various F and AF regions as a function of temperature. At the lowest temperatures (1.6 K) disordered spin-glass-like magnetic regions, which correspond to broad AF and F spectral features are identified. These regions are likely to comprise extended surface or boundary layers between the F and AF components which are important in establishing EB effects. As the temperature is raised from 1.6 K to 10 K the S spins in these *disordered* regions become dynamic on the NMR timescale and their contributions to the ^{55}Mn spectra decrease and, together with half of the nominally *ordered* F signal, are no longer detected above 10 K. The magnetically ordered material, which persists above 10 K, is comprised of nanoscale F and AF regions. For discussion purposes, the high-T F regions are tentatively classified as superparamagnetic F clusters, although their shape may not be simply spheroidal. The AF regions involve extended structures which constitute a matrix for the F clusters. The geometric nature of these regions could include chain or ribbon structures.

If, for simplicity in modeling, it is assumed that the F clusters are spheroidal, with a dual-peaked size distribution, then estimates of the cluster diameters for these components, derived from blocking-temperature-like behavior, give values of ~ 1 - 2 nm for the diameters of small clusters and ~ 4 - 12 nm for the larger clusters. Similar estimates can be made for the AF components with the diameter of the large regions exceeding 10 nm. While these size estimates should be viewed with caution, they indicate different types of nanoscale magnetic ordering in distinct regions. The model that has been suggested in the literature for the martensitic phase of this alloy at low temperatures, which involves F clusters embedded in an AF matrix, is, in broad terms, supported by our results. The NMR approach, however, provides fresh insights into the nature of the nanoscale spin substructures and the associated spin dynamics in this Ni$_2$Mn$_1$Sn$_1$ alloy. The technique and analysis procedures are applicable to other magnetic alloys.

Acknowledgments

The work at the National High Magnetic Field Laboratory is supported by NSF DMR-1157490 and by the State of Florida. JSB received funding from NSF-DMR 1309146. Work at UMN in CL's group supported by DOE under award DE-FG02-06ER46275. Work at UMN in RDJ's group supported by AFOSR-MURI (FA9550-12-1-0458), NSF-PIRE (OISE-0967140) and ONR (N00014-14-1-0714). The assistance of Daniel Phelan with sample fabrication is gratefully acknowledged.

APPENDIX A: INTRA-CLUSTER NMR RELAXATION MECHANISMS

We consider contributions to the ^{55}Mn longitudinal and transverse relaxation rates due to the fluctuating hyperfine field in a cluster of volume V at temperatures $T << T_B$. In general the nuclear relaxation rates for coupled electron-nuclear spin systems are given by the following expressions $1/T_1 = 2J^{(1)}(\omega_I)$ and $1/T_2 = J^{(1)}(\omega_I) + \frac{1}{2}J^{(0)}(0)$ where $J^{(1)}(\omega_I)$ and $J^{(0)}(0)$ are the spectral functions which correspond, respectively, to the transverse and longitudinal hyperfine field fluctuations at the nuclear Larmor frequency, ω_I, and at low frequencies, $\omega \to 0$ [37]. The two spectral densities are obtained as the Fourier transforms of the transverse, $G^{(1)}(t)$, and longitudinal, $G^{(0)}(t)$, time correlation functions of the interactions of the *S* and *I* spins. It is important to distinguish between processes which are secular, and do not involve energy exchange between nuclei and the lattice, and nonsecular processes which do involve *I* spin energy transfer to the lattice *via* the *S* spins. The transverse correlation function involves the raising and lowering spin operators S_+ and S_- in considering dynamic processes which involve *S* spin-flip transitions associated with spin wave excitations. Processes of this kind are unimportant in the correlated spin clusters for $T < T_B$ and the collective oscillations therefore make no contribution to spin-lattice relaxation and can be ignored.

The correlation function $G^{(0)}(t)$ has the form $G^{(0)}(t) = \left|\Delta A_z(T)/\hbar\right|^2 \left\langle S_z(0) S_z(t) \exp\left(-i\omega_S t\right)\right\rangle$ where the angular brackets represent a lattice average, $\omega_S = 2\pi/\tau_0$ and $\left|\Delta A_z/\hbar\right|^2 = \left(A/\hbar\right)^2 \left(1-\cos\theta_m(T)\right)^2 \approx \frac{1}{4}\left(A/\hbar\right)^2 \theta_m(T)^4$ with $\theta_m(T)^2 = K_A V/k_B T$ from Section IIIB. The spin cluster collective oscillations with frequency ω_S will undergo *changes in amplitude and phase* as a result of interactions with the phonon bath. Introducing a correlation time τ_c to describe dephasing processes of this kind gives $G^{(0)}(t) = \frac{1}{12}\left(A/\hbar\right)^2 \theta_m(T)^4 \left[S(S+1)\right] \exp\left(i\omega_S t\right) \exp\left(-t/\tau_c\right)$. The Fourier transform of the correlation function gives the spectral density and hence

$$\frac{1}{T_2} = \tfrac{1}{12} S(S+1)\omega_I^2 \left(\frac{k_B T}{K_A V}\right)^2 \left(\frac{\tau_c}{1+\omega_S^2 \tau_c^2}\right). \quad \text{(A1)}$$

If we take $S = 2$ for the Mn ions and adopt the long correlation time limit $\omega_S \tau_C > 1$, which corresponds to $\tau_C > \tau_0$, Eq. (A1) takes the form

$$\frac{1}{T_2} = \tfrac{1}{2}\left(\frac{\omega_I^2}{\omega_S^2}\right)\left(\frac{k_B T}{K_A V}\right)^2 \left(\frac{1}{\tau_c}\right). \quad \text{(A2)}$$

Spin-spin relaxation is of central importance in the present hyperfine NMR experiments since the contribution of nuclei in a given cluster to the spin-echo signal decreases to zero as $T_2 \rightarrow \tau_m^{NMR}$.

APPENDIX B: NMR SPIN-LATTICE RELAXATION IN MAGNETIC CLUSTERS

Since intra-cluster fluctuations in the hyperfine field do not contribute to spin-lattice relaxation, as pointed out in Appendix A, two other ^{55}Mn spin-lattice relaxation mechanisms are considered, as described in Section III D. These are firstly the inter-cluster fluctuating dipolar field mechanism and secondly the Korringa mechanism *via* the itinerant conduction electrons. Both mechanisms are found to contribute to ^{55}Mn spin-lattice relaxation in $Ni_{50}Mn_{40}Sn_{10}$ with the metallic Korringa process of dominant importance above 20 K, where large clusters contribute the major portion of the measured NMR signal, while the inter-cluster fluctuating dipolar field mechanism is of primary importance at lower temperatures.

We introduce the quantities $F_{sc}(T)$ and $F_{lc}(T)$ to represent the temperature dependent fractions of small cluster, denoted *sc*, and large cluster, *lc*, which together contribute to the NMR spin-echo signals. At the lowest temperatures (T <10 K) we have $F_{sc} > F_{lc}$ and the intercluster dipolar mediated mechanism is dominant while at higher temperatures $F_{sc} < F_{lc}$ and the Korringa-Moriya mechanism prevails.

In the intercluster case the dynamical matrix or shell surrounding a *frozen* cluster serves as a thermal bath in the relaxation process. It is the fluctuating transverse dipolar field component $B_{\perp}$, perpendicular to B_{hf}, that provides the longitudinal relaxation mechanism. Using Redfield theory [38], and with allowance for a distribution of correlation times corresponding to a distribution of sizes of small clusters, the relaxation rate is given by the following expression involving the nuclear Larmor frequency $\omega = \gamma B_{hf}$ (~ 2 x10^9 s^{-1}),

$$\frac{1}{T_1^{inter}} = \int_0^{\infty} \gamma^2 B_{\perp}^2 \left[\frac{\tau}{1+\omega^2\tau^2} \right] P(\tau) d\tau \ . \qquad \text{(B1)}$$

The integral involves fluctuating dipolar field contributions from neighbor dynamic clusters which undergo frequent180^o flips. The flip correlation time τ for a particular small cluster is given by the Néel-Arrhenius expression in terms of the cluster volume V and the anisotropy energy density K_A. This allows the integral to be expressed as a volume integral.

The Korringa-like relaxation rate expression for ferromagnetic metals in which the *orbital* processes have been shown to be of dominant importance is given by [39,40]

$$\frac{1}{T_1^K} = C \left\langle \frac{1}{r_A^3} \right\rangle_F \left(\rho_{\uparrow}^2 + \rho_{\downarrow}^2 \right) F(\Gamma) \ , \qquad \text{(B2)}$$

where $C = (16\pi/5)\mu_0^2\gamma_I^2\mu_B^2\hbar k_B T$ with μ_B the Bohr magneton, γ_I the nuclear gyromagnetic ratio and $\rho_{\uparrow}$ and $\rho_{\downarrow}$ the densities of states at the Fermi energy, E_F, for spin up and spin down electrons respectively. The inverse radius cubed $\left\langle 1/r_A^3 \right\rangle_F$ is averaged over the Fermi surface of the *d* band. The function $F(\Gamma)$ gives a measure of the t_{2g} orbital admixture in the wave function at E_F, with a maximum value of unity, for an equal admixture of t_{2g} and e_g orbitals, and a gradual decrease with departures from this condition. We take $F(\Gamma) = 1$ as an approximation in estimating the density of states at the Fermi level using Eq. (B2). .

References

1 *Magnetism and Structure in Functional Materials*, Edited by A. Planes, L. Mañosa, and A. Saxena, Vol.79 (Springer, New York 2005).

2 K. Ullako, J.K. Huang, C. Kantner, and R.C. O'Handley, Appl. Phys. Lett. **69**, 1966 (1996).

3 T. Krenke, E. Duman, M. Acet, E.F. Wassermann, X. Moya, L. Mañosa, and A. Planes, Nat. Mater. **4**, 450 (2005).

4 Y. Sutou, Y. Imano, N. Koeda, T.Omori, R. Kainuma, K. Ishida and K. Oikawa, Appl. Phys. Lett. **85**, 4358 (2004).

5 T. Krenke, M. Acet, E.F. Wassermann, X. Moya, L. Manosa and A. Planes, Phys. Rev. B **72**, 014412 (2005).

6 T. Krenke, M. Acet, E.F. Wassermann, X. Moya, L. Manosa and A. Planes, Phys. Rev. B **73**, 174413 (2006).

7 P. Entel, M. Siewert, M.E. Gruner, H.C. Herper, D. Comtesse, R. Arróyave, N. Singh, A. Talapatra, V. Sokolovskiy, V.D. Buchelnikov, F. Albertini, L. Righi, and V.A. Chernenko, Eur. Phys. J. B **86**, 65 (2013).

8 M. Khan, I. Dubenko, S. Stadler and N. Ali, J. Phys. Condens. Matter **20**, 235204 (2008).

9 S. Aksoy, M. Acet, P.P. Deen, L. Mañosa and A. Planes, Phys. Rev. B **79**, 212401 (2009).

10 M.Ye, A. Kimura, Y. Miura, M. Shirai, Y.T. Cui, K. Shimada, H. Namatame, M. Taniguchi, S. Ueda, K. Kobayashi, R. Kainuma, T. Shishido, K. Fukushima, and T. Kanomata, Phys. Rev. Lett. **104**, 176401 (2010).

11 S.J. Murray, M. Marioni, S.M. Allen and R.C. O'Handley, Appl. Phys. Lett. **77**, 886 (2000).

12 I. Benichou, E. Faran, D. Shilo and S. Givli, Appl. Phys. Lett. **102**, 011912 (2013).

13 R.I. Barabash, C. Kirchlechner, O. Robach, O. Ulrich, J-S. Micha, A. Sozinov and O.M. Barabash, Appl. Phys. Lett. **103**, 021909 (2013).

14 K. P. Bhatti, S. El-Khatib, V. Srivistava, R.D. James and C. Leighton, Phys. Rev. B **85**, 134450 (2012).

15 M. Khan, I. Dubenko, s. Stadler and N. Ali, J. Appl. Phys. **102**, 113914 (2007).

16 M. Khan, I. Dubenko, S. Stadler and N. Ali, Appl. Phys. Lett. **91**, 072510 (2007).

17 Z. Li, C. Jing, J. Chen, S. Yuan, S. Cao and J. Zhang, Appl. Phys. Lett. **91**, 112505 (2007).

18 B.M. Wang, Y. Liu, P. Ren, B. Xia, K.B. Ruan, J.B. Yi, J. Ding, X.G. Li and L. Wang, Phys. Rev. Lett. **106**, 077203 (2011).

19 S. Ishida, Y. Kubo, J. Ishida and S. Asano, J. Phys. Soc. Japan **48**, 814 (1980).

20 J. Kübler, A.R. Williams and C. B. Sommers, Phys. Rev. B **28**, 1745 (1983).

21 A. Ayuela, J. Enkovaara, K. Ullakko and R. M. Niemenen, J. Phys. Condens. Matter **11**, 2017 (1999).

22 S. Fujii, S. Ishida and S. Sasano, J. Phys. Soc. Japan **58**, 3657 (1989).

23 P.J. Brown, A.Y. Bargawi, J. Crangle, K-U Neumann and K.R.A. Ziebeck, J. Phys. Condens. Matter **11**, 4715 (1999).

24 S.M. Podgornykh, S.V. Strelsov, V.A. Kazantsev and E.I. Shreder, Third Moscow International Symposium on Magnetism Proceedings, 194 (2005).

25 D.Y. Cong, S. Roth, M. Pötschke, C. Hürrich and L. Schultz, Appl. Phys. Lett. **97**, 021908 (2010).

26 K.P. Bhatti, V. Srivastava, D.P. Phelan, S. El-Khatib, R.D. James and C. Leighton in *Heusler Alloys*, edited by A. Hirohata and C. Felser (Springer, 2015).

27 R. Kainuma, Y. Imano, W. Ito, H. Morito, Y. Sutou, K. Oikawa, A. Fujita, K. Ishida, S. Okamoto and O. Kitakami, Appl. Phys. Lett. **88**, 192513 (2006).

28 R. Kainuma, Y. Imano, W. Ito, Y. Sutou, H. Morito, S. Okamoto, O. Kitakami, K. Oikawa, A. Fujita, T. Kanomata and K. Ishida, Nature **439**, 957 (2006).

29 V. Srivastava, X. Chen, and R.D. James, Appl. Phys. Lett. **97**, 014101 (2010).

30 W. Ito, X. Xu, R.Y. Umetsu, T. Kanomata, K. Ishida, and R. Kainuma, Appl. Phys. Lett. **97**, 242512 (2010).

31 D.Y. Cong, S. Roth, and L. Schultz, Acta Materialia **60**, 5335 (2012).

32 R. E. Watson, and A.J. Freeman, Phys. Rev. **123**, 2027 (1961).

33 M. Belesi, L. Giebeler, C.G.F. Blum, B. Büchner, and S. Wurmehl, Phys. Rev. B **91**, 134415 (2015).

34 T. Shiohara, J. Phys. Soc. Japan **28**, 313 (1970).

35 M.F. Hansen, C.B. Koch and S. Mørup, Phys. Rev. B **62**, 1124 (2000).

36 L.T. Kuhn, K. Lefmann, C.R.H. Bahl, S.N. Ancona, P.-A. Linfg□rd, C. Frandsen, D.E. Madsen, and S. Mørup, Phys. Rev. B **74**, 184406 (2006).

37 A. Abragam, *The Principles of Nuclear Magnetism*, (Oxford University Press, 1961) p. 311.

38 C.P. Slichter, *Principles of Magnetic Resonance*, 3 rd ed. (Springer Verlag, Heidelberg, 1996).

39 Y. Obata, J. Phys. Soc. Japan,**18**, 1020 (1963).

40 T. Moriya, J. Phys. Soc. Japan, **19**, 681 (1964).

Figure captions

FIG. 1 (Color online). (a) Crystal structure of the cubic ordered Heusler alloy $Ni_{50}Mn_{25}Sn_{25}$ (*i.e.* Ni_2MnSn) in the austenite phase. (b) Representation of ferromagnetic exchange interactions which couple nearest neighbor Mn atoms at sites 1 and 2 in the (001) plane of $Ni_{50}Mn_{25}Sn_{25}$. (c) Incorporation of additional Mn, together with a reduction in Sn, gives $Ni_{50}Mn_{50-x}Sn_x$, and results in antiferromagnetic exchange interactions between the new nearest-neighbor Mn atoms 1 and 3, as depicted. For simplicity small structural changes produced by changes in x are ignored.

FIG. 2. Curie law corrected (T-scaled) ^{55}Mn zero field cooled and zero field measured ^{55}Mn hyperfine spectra for $Ni_{50}Mn_{40}Sn_{10}$ at temperatures in the range 1.6 – 320 K. The spectral components centered at 248 MHz are identified as AF while the components at frequencies above 280 MHz are F. In contrast to the AF component frequencies, which remain roughly constant, the frequencies of the F components are temperature-dependent.

FIG. 3 (Color online). (a) The F (f_{hf} > 275 MHz) and AF (f_{hf} < 275 MHz) best-fit Gaussian spectral components to the 1.6 K ^{55}Mn spectrum which are shown with the fit curves in Fig. 3 (b). The AF components comprise a narrow line (AF2) with shoulders (AF1 and AF3), which persist to high temperature (300 K), and an underlying broad line (AF4) that decays in amplitude as the temperature is raised and cannot be detected above 10 K due to spin dynamics, as discussed in the text. The F signals involve narrow components at 284 MHz, 309 MHz and 334 MHz (F1, F2 and F3) and a broad F component (F4) which underlies the narrow peaks. The narrow components reduce somewhat in amplitude with increasing temperature, and can no longer be detected above 300 K. The broad component F4 is not seen above 10 K due to dynamical effects.

FIG. 4 (Color online). The temperature dependence of the ^{55}Mn NMR center frequencies of the F2, F3 and AF2 spectral components for $Ni_{50}Mn_{40}Sn_{10}$ as depicted in Fig. 2. The F2 and F3 components shift down in frequency with increasing temperature, while the frequency of AF2 remains essentially constant to 340 K. The linear fit to the low temperature F3 data provides an estimate of the large cluster energy density as discussed in the text. The curves through the points are spline fits to guide the eye. The inset shows an expanded plot of the low temperature region for F3.

FIG. 5 (Color online). The center frequencies of the narrow F and AF ^{55}Mn spectral components for $Ni_{50}Mn_{40}Sn_{10}$ shown as a function of applied field, $\mu_0 H$, at 1.6 K. The slope of the straight lines through the plotted points for comp[onents F1, F2 and F3 is $-{}^{55}\gamma = -10.5$ MHz/T, as predicted for the F regions. The frequency of AF2 increases gradually for $0 < \mu_0 H < 1$ T and then more rapidly for $\mu_0 H > 1$ T, consistent with a spin-flop transition followed by canting of the spins above 1 T as discussed in the text.

FIG. 6 (Color online). The curves labeled F (red triangles) are the temperature-scaled (Curie law corrected) spectral areas, for the F (F1, F2, F3 and F4, (f_{hf} > 270 MHz)) components in $Ni_{50}Mn_{40}Sn_{10}$ for $\mu_0 H = 0$ T and 1T. The scaled areas are proportional to the number of contributing ^{55}Mn spins. The applied field of 1T produces little change in the evolution of the spectral area with T. The curves labeled AF (black triangles) are the temperature-scaled areas for the AF components (AF1, AF2, AF3 and AF4, (f_{hf} < 270 MHz)) for $\mu_0 H = 0$ T and 1T. Following a marked decrease in the temperature-scaled areas for both F and AF components in the range 2 to 10 K, plateaus occur between 10 and 150 K. The fitted

curves for the F (full line) and the AF (dash line) components for 0 T are obtained by integrating over bimodal distributions of cluster sizes. As a simplification the spin clusters are assumed to be spheroidal with a distribution of NMR blocking temperatures as discussed in the text. The 1T applied field produces only small changes in the spectral area behavior with temperature.

FIG. 7 (Color online). The ^{55}Mn spin-lattice relaxation times T_1 versus temperature (log scale) in $Ni_{50}Mn_{40}Sn_{10}$ for applied fields of 0 T and 1 T at frequencies corresponding to (a) the F3 plus F4 components (red upward triangles) and (b) the AF2 plus AF4 components (black downward triangles). The curves that are fit to the 0 T data involve a cluster size distribution as discussed in the text. The insets show the temperature dependence of the exponent β obtained in the fit of the nuclear magnetization recovery curves with stretched exponentials.

FIG. 8 (Color online). The ^{55}Mn spin-spin relaxation times T_2 versus temperature (log scale) for $Ni_{50}Mn_{40}Sn_{10}$ in zero applied field at frequencies corresponding to (a) the F3 plus F4 components (red upward triangles) and (b) the AF2 plus AF4 components (black downward triangles). The curves through the data are simply guides to the eye. The insets show the temperature dependence of the exponent β obtained in the fit of the ^{55}Mn spin-echo decay curves with stretched exponentials.

FIG. 9 (Color online). Korringa-style plots of $1/T_1T$ versus T for the 0 T and 1 T data shown in Fig. 7 at frequencies corresponding to (a) the F3 plus F4 components (in units ms^{-1} K^{-1}, red upward triangles) and (b) the AF2 plus AF4 components (in units s^{-1} K^{-1}, black downward triangles). The fit curves involve the cluster size distribution used in Fig. 7, as discussed in the text. Korringa relaxation, as given by Eq. (5), applies to both F and AF components at $T > 20$ K.

Figures

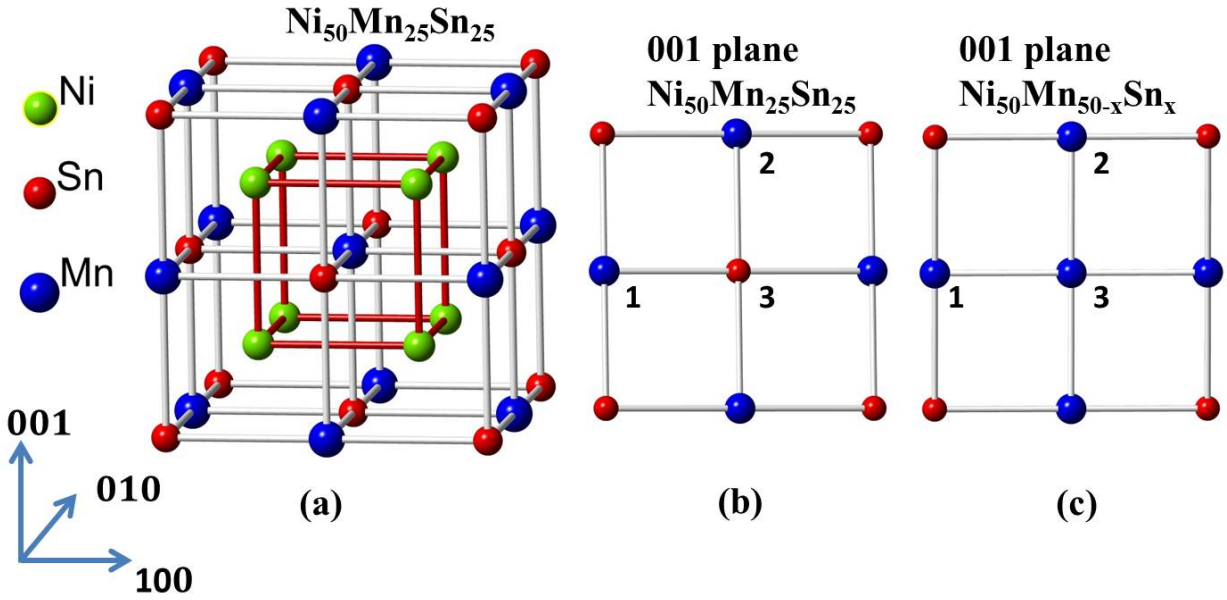

FIG. 1

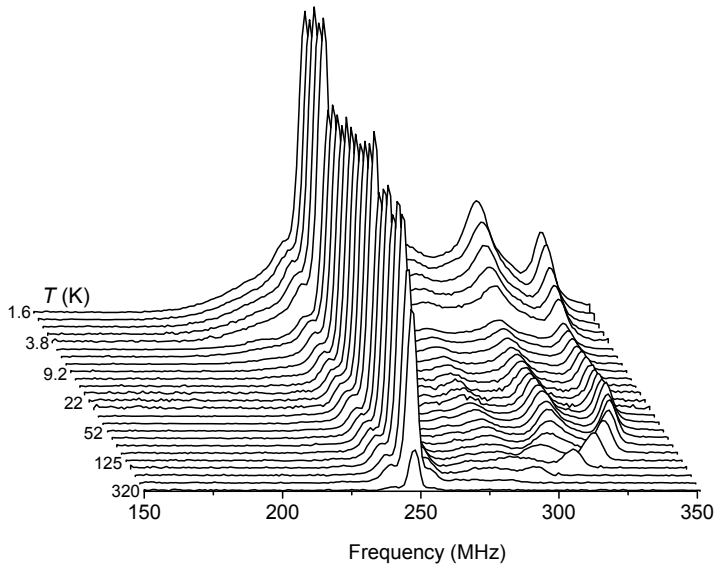

FIG. 2

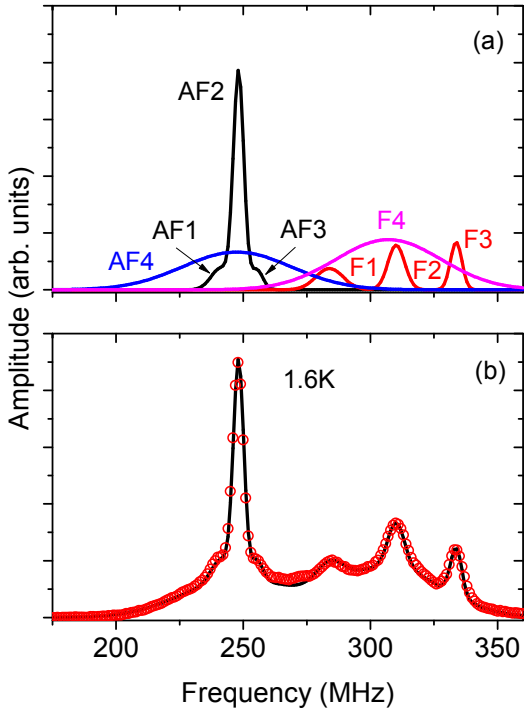
(a)
AF2
AF1
AF3
F4
F3
AF4
F1
F2
Amplitude (arb. units)
1.6K
(b)
200
250
300
350
Frequency (MHz)

FIG. 3

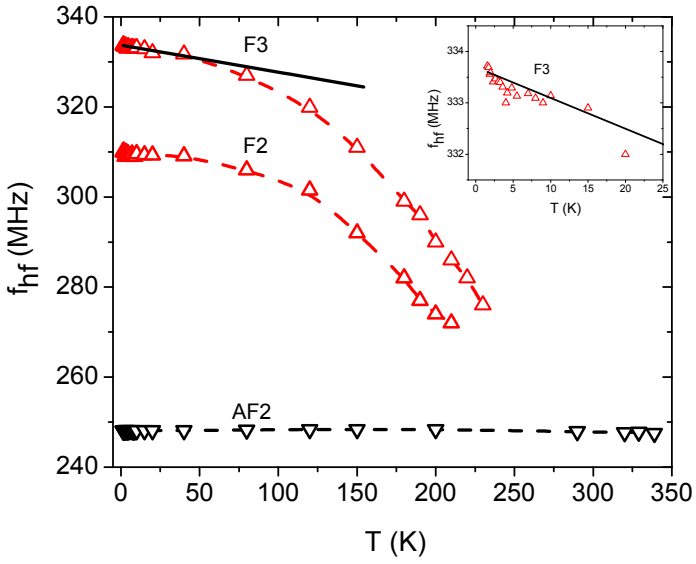
340
320
300
280
260
240
F3
F2
AF2
f_{hf} (MHz)
0
50
100
150
200
250
300
350
T (K)
334
333
332
F3
f_{hf} (MHz)
0
5
10
15
20
25
T (K)

FIG. 4

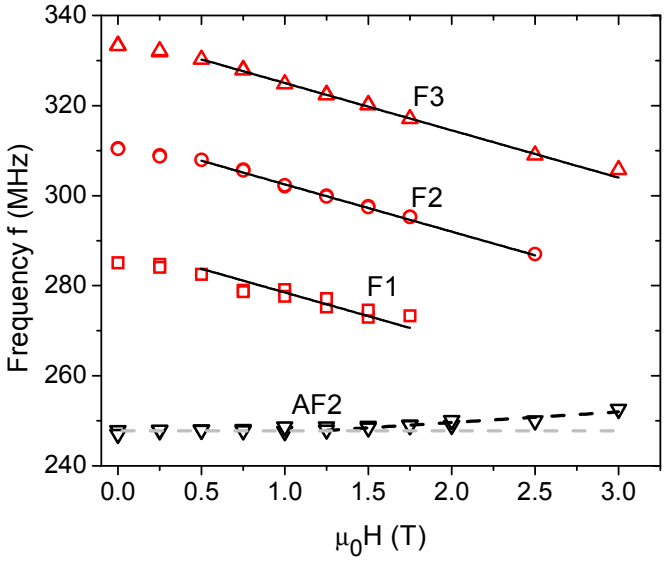
340
320
300
280
260
240
Frequency f (MHz)
F3
F2
F1
AF2
0.0
0.5
1.0
1.5
2.0
2.5
3.0
μ0H (T)

FIG. 5

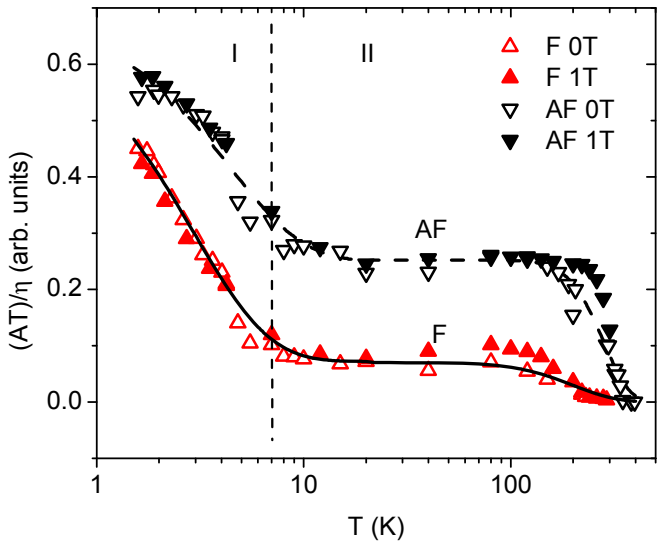
I
II
F 0T
F 1T
AF 0T
AF 1T
AF
F
0.6
0.4
0.2
0.0
(AT)/η (arb. units)
1
10
100
T (K)

FIG. 6

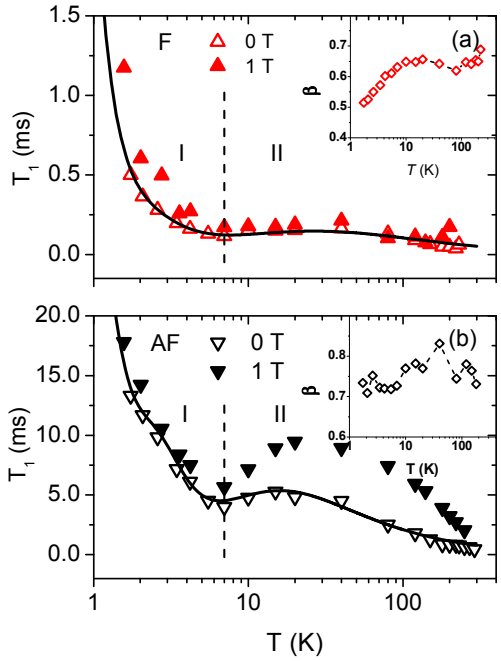
F
0 T
1 T
(a)
I
II
β
T (K)
T$_1$ (ms)
AF
0 T
1 T
(b)
I
II
β
T (K)
T$_1$ (ms)
T (K)

FIG. 7

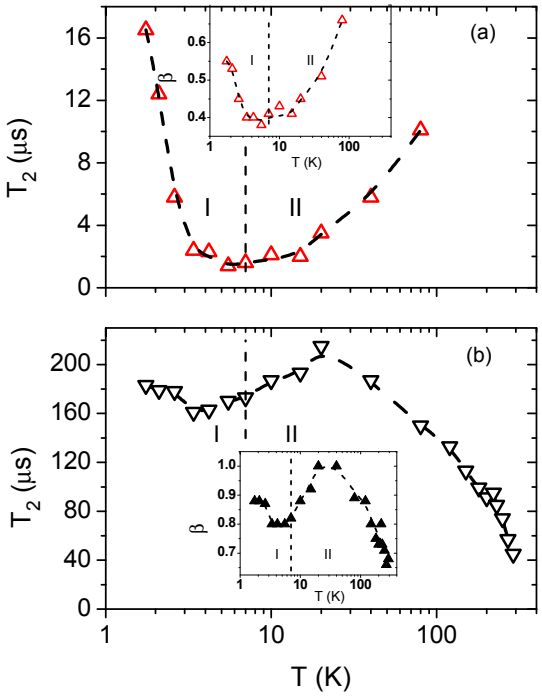
(a)
β
I
II
T (K)
T$_2$ (μs)
(b)
I
II
β
T (K)
T$_2$ (μs)
T (K)

FIG. 8

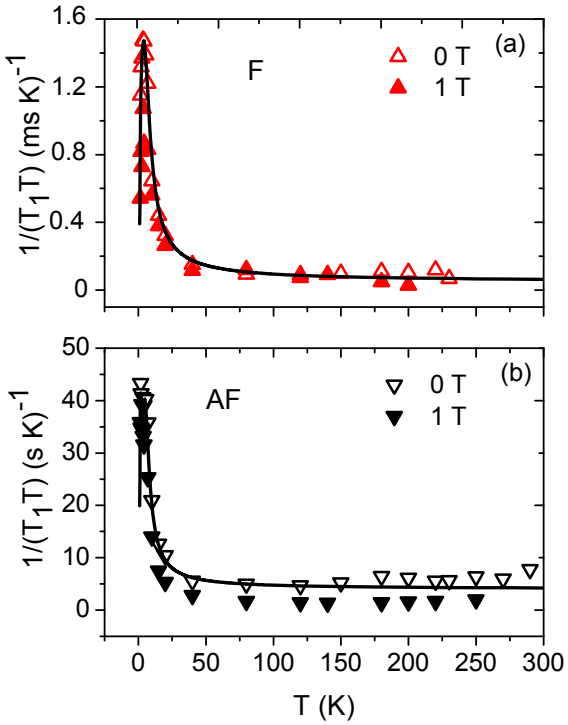
1.6
1.2
0.8
0.4
0
1/(T1T) (ms K)-1
F
0 T
1 T
(a)
50
40
30
20
10
0
1/(T1T) (s K)-1
AF
0 T
1 T
(b)
0
50
100
150
200
250
300
T (K)

FIG. 9